ADVANCED MATERIALS
www.advmat.de

Bond Confinement-Dependent Peierls Distortion in Epitaxially Grown Bismuth Films

*Felix Hoff, Peter Kerres, Timo Veslin, Abdur Rehman Jalil, Thomas Schmidt, Simone Ritarossi, Jan Köttgen, Lucas Bothe, Jonathan Frank, Carl-Friedrich Schön, Yazhi Xu, Dasol Kim, Julian Mertens, Joachim Mayer, Riccardo Mazzarello, and Matthias Wuttig**

A systematic study of the impact of film thickness on the properties of thin Bi films is presented. To this end, epitaxial films of high quality have been grown on a Si (111) substrate with thicknesses ranging from 1.9 to 29.9 nm. Broadband optical spectroscopy reveals a notable decline in the optical dielectric constant and the absorption peak height as the film thickness decreases, alongside a shift of the absorption maximum to higher photon energies. Raman and pump-probe spectroscopy show that the phonon mode frequencies increase upon decreasing film thickness, with the in-plane mode frequency rising by 10% from the thickest to the thinnest sample. The X-ray diffraction analysis reveals an increasing Peierls distortion for thinner films, explaining the observed property changes. Quantum chemical bonding analysis and density functional theory calculations show that the properties of thin bismuth are influenced by the interplay between electron localization and delocalization, characteristic of metavalently bonded solids. This study shows that for solids that utilize metavalent bonding, a thickness reduction leads to significant property changes. The effect can even be employed to tailor material properties without the need to change material stoichiometry.

1. Introduction

The exploration of monoatomic single-layer 2D materials has significantly broadened the portfolio of properties and applications of monoatomic materials. Over the past decade, the group of 2D pnictogens has emerged, alongside well-known graphene[1,2] and has revealed surprising material properties. A recent study, for example, has shown 2D ferroelectricity in single-element bismuthene.[3] Furthermore, calculations and measurements have demonstrated that monolayer bismuth exhibits impressive thermoelectric properties, showing a high figure of merit.[4,5] Within this monolayer, the material adopts a buckled honeycomb structure. In addition, bismuth has been shown to behave as a quantum spin Hall insulator, making it an interesting 2D topological insulator.[6–8] Besides the recent discoveries concerning 2D bismuth, ongoing research is revealing new potential applications for the bulk material, including the observation of superconductivity in single crystals at ambient pressure[9] and its use as material in battery technology.[10] The simple synthesis of bismuth nanoparticles extends these ranges even further.[11]

Interestingly, there is a fundamental difference between graphene and bismuthene. Multilayer graphene (if not twisted) employs weak coupling between adjacent layers. Hence, the properties do not change drastically upon the transition from monolayer films to bulk samples. This is very different for

F. Hoff, T. Veslin, T. Schmidt, J. Köttgen, J. Frank, C.-F. Schön, D. Kim, J. Mertens, M. Wuttig
Institute of Physics (IA)
RWTH Aachen University
Sommerfeldstraße 14, 52074 Aachen, Germany
E-mail: wuttig@physik.rwth-aachen.de

The ORCID identification number(s) for the author(s) of this article can be found under https://doi.org/10.1002/adma.202416938

DOI: 10.1002/adma.202416938

P. Kerres, A. R. Jalil, L. Bothe, M. Wuttig
Peter Grünberg Institute – JARA-Institute Energy Efficient Information Technology (PGI-10)
Wilhelm-Johnen-Straße, 52428 Jülich, Germany

S. Ritarossi, R. Mazzarello
Dipartimento di Fisica
Sapienza University of Rome
Piazzale Aldo Moro 5, Rome 00185, Italy

Y. Xu
Department of Applied Physics
School of Science
Chang'an University
Xi'an 710064, China

J. Mayer
Central Facility for Electron Microscopy
RWTH Aachen University
Ahornstr. 55, 52074 Aachen, Germany

bismuth, which is a semiconductor as a monolayer, but a semimetal as a thick film / bulk sample.[12] Hence, we expect to find pronounced property changes in films with increasing film thickness. The investigation and subsequent understanding of property changes as a function of film thickness is the goal of the present study.

Notably, recent research on properties predominantly focuses either on the monolayer 2D material realm or on bulk materials. The transition from bulk to monolayer materials is rarely discussed, and when it is, studies tend to concentrate on individual properties or measurement techniques like ellipsometry[13] or electrical transport.[14] A thorough investigation of the development of property trends and the underlying origin, however, have not yet been the focus of investigation. Since bismuth serves as a quintessential model system in femtosecond (fs) pump-probe spectroscopy, owing to its structural sensitivity toward ultrafast charge carrier excitation,[15–18] thin films have been probed extensively using fs pump-probe methodology.[19–21] On the one hand these observations spark considerable interest to exploit bismuth as a functional material platform.[22] On the other hand, a comprehensive understanding of the bulk-to-monolayer transition is still missing. This is the focus of the present investigation.

With this goal in mind, we have fabricated Bi films using molecular beam epitaxy (MBE) to guarantee optimal crystalline texture and film quality. Our focus has been on layer thicknesses below 10 nm, with some thicker layers included. The study employed broadband optical characterization across a broad spectral range to ascertain the dielectric properties of the thin films. Additionally, the dynamics of light-matter interaction on ultrashort time scales and the corresponding lattice dynamics were investigated using anisotropic optical fs pump-probe spectroscopy and Raman spectroscopy. Moreover, we utilized advanced structural analysis techniques. This approach allows for a comprehensive examination of the Peierls distortion, with a particular focus on the ratio of long to short bonds. The structural distortion of the material is intricately linked with its electronic band structure, thereby directly influencing its physical properties. Furthermore, a quantum chemical bonding analysis was conducted to elucidate the bonding mechanism within the material.

2. Results

2.1. Epitaxially Grown Ultrathin Bismuth Films

Ultrathin bismuth films were produced via MBE on a Si (111) 1×1 – Bi terminated surface. During this process, a total of 15 samples were generated, covering a film thickness range from 1.9 to 29.9 nm. The 1×1 Bi passivation layer creates an incoherent interface, as can be observed in the transmission electron microscopy (TEM) image in **Figure 1a**.[23,24] The large distance between Bi film and passivation layer implies that the underlying coupling is very weak. The weak coupling prevents formation of a significant strain in the Bi film. The resulting incoherence of the interface is also evidenced by the absence of misfit dislocations, which would be expected for the existing lateral lattice mismatch of 18% and the deposited film thickness, which is certainly above the critical thickness for strain relaxation. This is in contrast to the behavior observed in $\sqrt{3} \times \sqrt{3} - \beta$ Bi or 7×7 Bi reconstructed surfaces, for which a significant strain has been reported.[25–28] Structural characterization of our samples has been performed using X-ray diffraction (XRD). The measured θ–2θ diffractograms illustrated in Figure 1b, show the excellent texture of all films, as demonstrated by the exclusive presence of trigonal (0003n) peaks across all samples. This shows that all films grow with trigonal structure. Owing to the high smoothness and crystalline quality of the thin films, Laue oscillations within the diffraction pattern remain visible up to a Q_z value of 5.25 $Å^{-1}$ and are without notable dephasing. This indicates an almost perfect alignment of the scattering planes perpendicular to the c-axis of the crystalline unit cell shown in Figure S1 (Supporting Information). A widening of the peaks with decreasing layer thickness is observable throughout the entire diffractogram. This phenomenon can be attributed to the finite size effect due to the small film thickness. The coherent scattering length derived from the Laue fringes corresponds to the mean film thickness obtained from X-ray reflectivity (XRR) measurements. This ensures a uniform optical response throughout the film, as all Bi bilayers are parallel to the surface. This uniformity is crucial to obtain a strong coherent phonon signal. Previous studies of samples grown with the same parameters[23] have shown that indeed a columnar growth without grain boundaries in the growth direction is observed. We have adopted these growth parameters for the present study.

The out-of-plane alignment of the films is investigated further through the use of reciprocal space maps (RSM) of the (0003n) peaks. $|Q|$ integrated profiles along ω demonstrate a high degree of grain alignment, as illustrated in Figure S1 (Supporting Information). The width of these peaks is a measure for the alignment of the (0003n) peaks parallel to the surface. A comparable full width at half maximum (FWHM) of ≈0.1 ° is observed for all samples, indicating that the film quality is similar for the full range of film thicknesses. This is corroborated by the peak width in the RSMs for four representative film thicknesses, as illustrated in Figure 1c–f. Figure S2 (Supporting Information) depicts scanning electron microscope (SEM) images of two samples of 1.5 and 12.5 nm thickness, which demonstrate a high surface quality of the epitaxial films. Electron backscattering diffraction (EBSD) measurements were conducted to examine the in-plane texture and mean grain size. Figure S3 (Supporting Information) illustrates the resulting grain orientation map of the 12.5 nm sample. Two distinct in-plane orientations are evident: the dominant $(1\bar{1}00)$ orientation, which exhibits grains of multiple micrometers in size, and the less dominant $(0\bar{1}10)$ phase, which describes the twin domain. These domains are prominent in the φ-scan in Figure 1g, which also shows additional rotational domains at 27.5 and 30 , not detectable with XRD and EBSD in films thinner than 3.9 nm. An azimuthal RSM of the 8.9 nm sample (Figure S4, Supporting Information) provides further insight. In addition to the aforementioned domains, a residual fiber texture is present in the sample. Nevertheless, over 88% of the sample is covered by the primary and twin domains. As the other samples exhibit an even higher primary to rotational domain ratio, their alignment is even better. A further confirmation of this behavior is demonstrated by a grain orientation map with a higher resolution (Figure S3, Supporting Information).

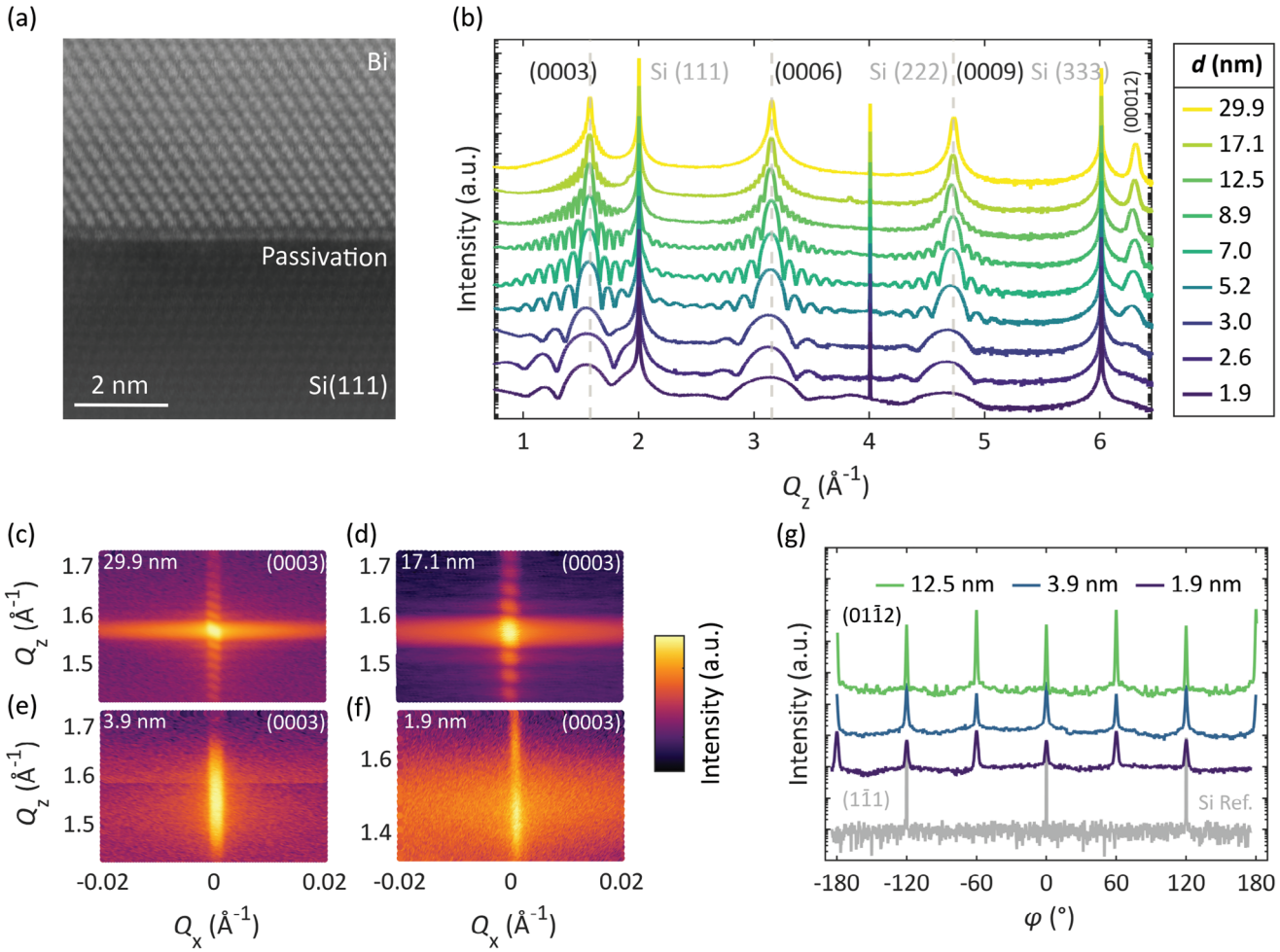

Figure 1. a) The STEM data of a bismuth film, namely a cross-sectional HAADF image acquired along the Si $(1\bar{1}0)$ projection, offers insights into the incoherent interface between Bi bilayers and the 1 × 1 Bi passivation layer. b) Various θ–2θ XRD data of the thin film series investigated. The films are grown epitaxially along the (0003n) direction. The existence and number of Laue oscillations is indicative of smooth and coherent growth. Peak shifts toward lower Q_z values show an increase in the c–axis for the thinnest samples. Symmetric reciprocal space maps across the (0003) peak for c) 29.9 nm d) 17.1 nm e) 3.9 nm, and f) 1.9 nm film thickness. g) Logarithmic plot of the φ scans of the $(01\bar{1}2)$ peak over 360° shows a biaxial texture with three peaks from the primary and three peaks from the twin domain. In the thicker films additional rotational domains can be seen which are much weaker.

2.2. Optical Response to the Decrease in Film Thickness

The high structural quality across the range of film thicknesses under investigation is beneficial for the subsequent determination of optical properties. It facilitates the exploration of various physical properties as a function of film thickness, since the impact of film imperfections can be ignored. In the following, optical properties will be presented and discussed, which have been measured over a broad spectral range from far-infrared to near-ultraviolet wavelengths. The measured reflectance data are shown in Figure S5 (Supporting Information). The results of the fitted reflectance data are presented as the real part (**Figure 2a**) and the imaginary part (Figure 2b) of the dielectric function for numerous film thicknesses.

To simplify a discussion of the interband transitions between 1 and 2 eV, the Drude contribution has been subtracted here. The data with the Drude contribution, as well as the Drude contribution only, of all thicknesses can be found in the supporting information.

At first, the optical dielectric constant ε_∞ is discussed. As depicted in Figure 2c, it is evident that ε_∞ decreases significantly upon decreasing film thickness. The optical dielectric constant ε_∞ is defined at frequencies significantly higher than the phonon resonance but lower than the next natural frequency of the crystal, which is associated with bound electronic transitions in the visible and ultraviolet regions. For non-metals, the reported values of ε_∞ are particularly high.[29–31]

Subsequently, attention is directed toward the height and the position of the absorption maximum. As shown in Figure 2d, $\varepsilon_2^{\max}$ reaches 100 for the thickest layers and progressively decreases to a value of ≈60 for thinner layers. Concomitantly, the energy $E(\varepsilon_2^{\max})$, at which the absorption maximum occurs shifts significantly from 0.8 to 1.2 eV for thinner layers.

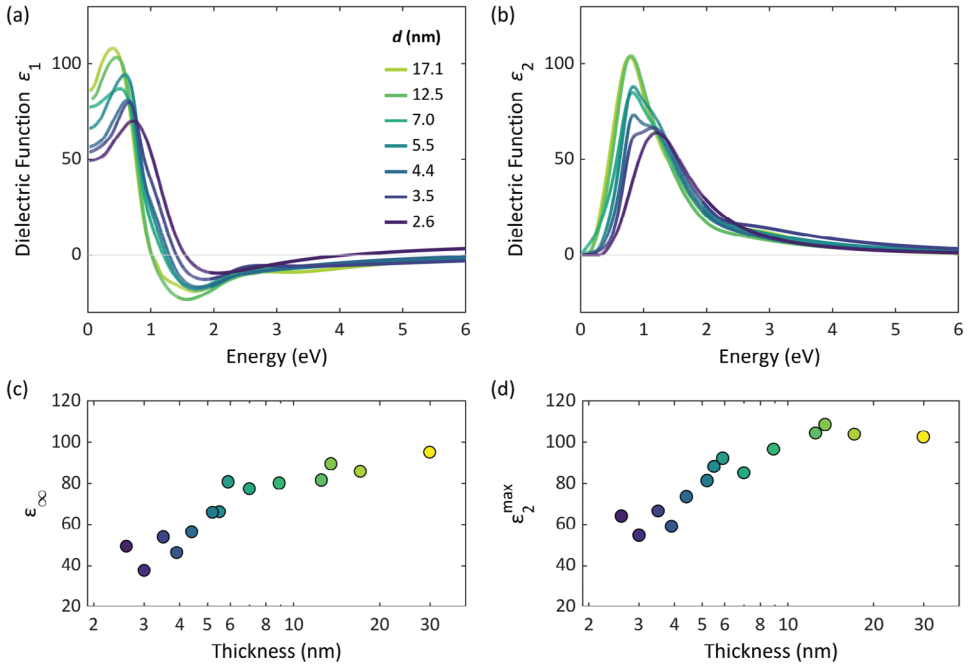

Figure 2. The real part a) and imaginary part b) of the dielectric function of various bismuth thin films obtained by optical spectroscopy. To focus on optical transitions in the visible spectrum, the Drude contribution is subtracted in both plots. c) The optical dielectric constant ϵ_∞ at the low frequency limit and d) the absorption maximum $\epsilon_2{}^{max}$ decrease sharply upon decreasing film thickness. The absorption maximum is blue-shifted toward thinner films.

2.3. Lattice Dynamics Response to the Decrease in Film Thickness

The changes observed for the dielectric function are indicative of changes of the electronic band structure with film thickness. Such changes are presumably governed by changes of bonding. Thus, both the photoexcitation process and the lattice dynamics are expected to undergo concomitant changes. To study these changes, transient reflectivity data are obtained, employing reflection type fs pump-probe measurements. Thus, insights into the dynamic response of charge carriers and the crystalline lattice to external stimuli can be determined. The measurements were conducted in both isotropic and anisotropic configurations (electro-optic (EO)-sampling),[32] covering a range of pump fluences, extending from 0.1 to 1.0 mJ cm^{-2}.

In **Figure 3a**, the isotropic transient reflectivity for various thin film samples is shown. Each curve is normalized to its maximum excitation amplitude and vertically shifted for clarity. The coherent excitation of the A_{1g} phonon mode is visible for all samples, even for the thinnest film. The entire set of data can be found in the supporting information.

In order to determine the frequency of the coherent phonons, we employed data fitting in the time domain, utilizing damped harmonic oscillations. Furthermore, three exponential contributions were incorporated to describe the response to electronic excitation and deexcitation, as well as lattice heating. The data aligns well with a damped harmonic oscillator model, enabling the identification of the phonon frequencies. This analysis is performed systematically on samples exposed to various pump fluences. As an example, the influence of the pump fluence is shown in the EO sampling of the 12.5 nm thick sample in Figure S10 (Supporting Information). A redshift of the A_{1g} and E_g phonon modes with increasing pump fluence is visible in the Fourier spectrum in the inset. Figure 3b illustrates the A_{1g} frequencies resulting from the damped oscillator fits plotted against the pump fluence shown exemplarily for four different thicknesses.

A linear relationship between fluence and mode frequency is evident. The magnitude of the frequency redshift varies with film thickness: it is moderate in the thickest samples, but more pronounced in the thinner samples. Specifically, the A_{1g} mode frequency of the 3.5 nm sample decreases by 20% by increasing the pump fluence from 0.1 to 0.7 mJ cm^{-2}. This effect diminishes slightly for the even thinner samples, whose frequencies are shifted to higher values in comparison to those of the 3.5 nm sample. To disentangle film thickness effects from pump fluence effects, these data points are extrapolated to a fluence approaching zero. To achieve this, a linear regression analysis is applied and shown as dashed lines. At the zero-fluence limit, a thickness-dependent phonon frequency blueshift is visible.

As a next step, Raman spectroscopy provides vibrational mode information without optical pre-excitation and thus directly probes the film thickness effect. The corresponding spectra of various thin films are depicted in Figure 3c. For the thickest samples, the Raman spectra exhibit two distinct peaks at 73 and 100 cm^{-1}, which can be attributed to the E_g and A_{1g} phonon modes, respectively.[33] For better comparability, each curve is normalized to the peak intensity of the E_g mode and shifted vertically. Dashed vertical lines pinned to the peak position of the thickest sample are shown.

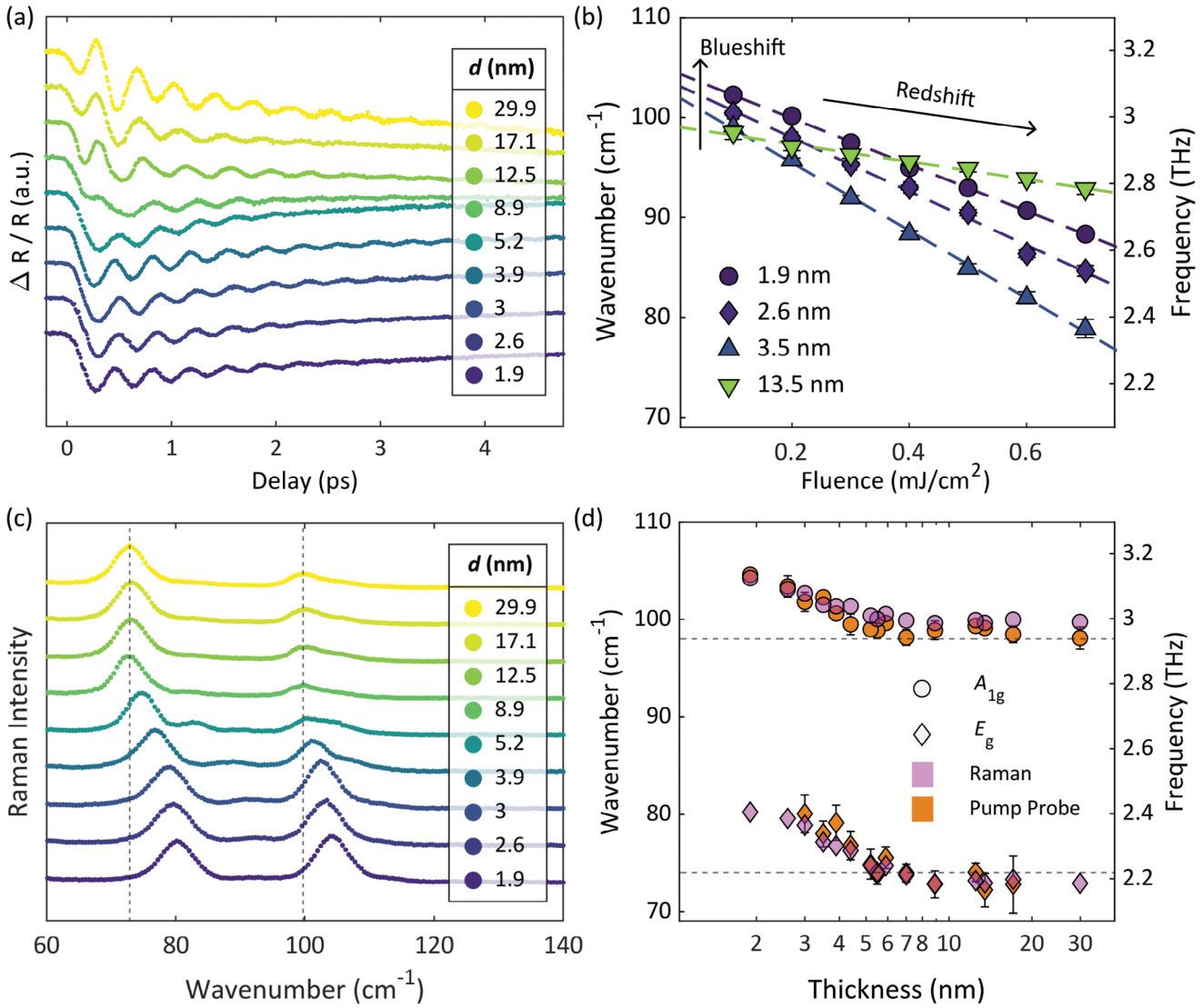

Figure 3. a) Isotropic transient reflectivity for a number of thin film samples. Each curve is normalized to its excitation amplitude and vertically shifted for clarity. The excitation of the coherent A_{1g} phonon mode is visible in each curve. b) The softening of the phonon mode for increasing excitation fluence is clearly recognizable for the layer thicknesses shown, but varies in magnitude. By extrapolating to vanishing fluence, a hardening of the mode toward smaller layer thicknesses is visible. c) Raman spectra derived from a variety of thin film samples, with each curve normalized to the peak intensity of the E_g mode and vertically displaced for improved visualization. Vertical lines are employed to indicate the Raman shift peak positions of the thickest sample. d) The Raman shift peak position of the predominant E_g mode (violet diamonds) unveils a significant phonon mode hardening as the layer thickness decreases below 7 nm. The same trend is evident for the second peak within the spectrum, revealing an increase in the frequency of the A_{1g} phonon mode (violet circles). Frequencies obtained by Lorentzian curve fitting. The same trend is obtained by zero-fluence extrapolation of the phonon softening of the transient reflectivity, shown in orange. Dashed horizontal lines represent the literature bulk values.[33]

It is noticeable that both modes undergo a blueshift when the film thickness is reduced. It can be seen that the frequency of the E_g mode changes more strongly upon reduction of film thickness than the A_{1g} mode. While the latter has a smaller amplitude for most samples, it becomes dominant for film thicknesses below 3.5 nm. Interestingly, this also denotes the range beyond which we are unable to discern the E_g mode using the EO sampling in real-time measurements. The detailed trend of the intensity ratio of both modes with respect to layer thickness as well as the measurements for all samples can be found in the supporting information.

Figure 3d presents the precise Raman peak positions of both modes with respect to the film thickness of the measured films, showing the substantial blueshift of the phonon modes with decreasing layer thickness. The resulting phonon frequencies of the Raman measurements are shown in light purple and the results of the zero fluence extrapolation (ZFE) pump probe analysis are shown in orange. Notably, the frequency of the E_g mode (diamonds) in the thinnest layer increases by 10% compared to the frequency in the thickest film. The increase starts when the thickness falls below 7 nm and persists continuously toward the thinnest film thicknesses. A similar trend is evident for the

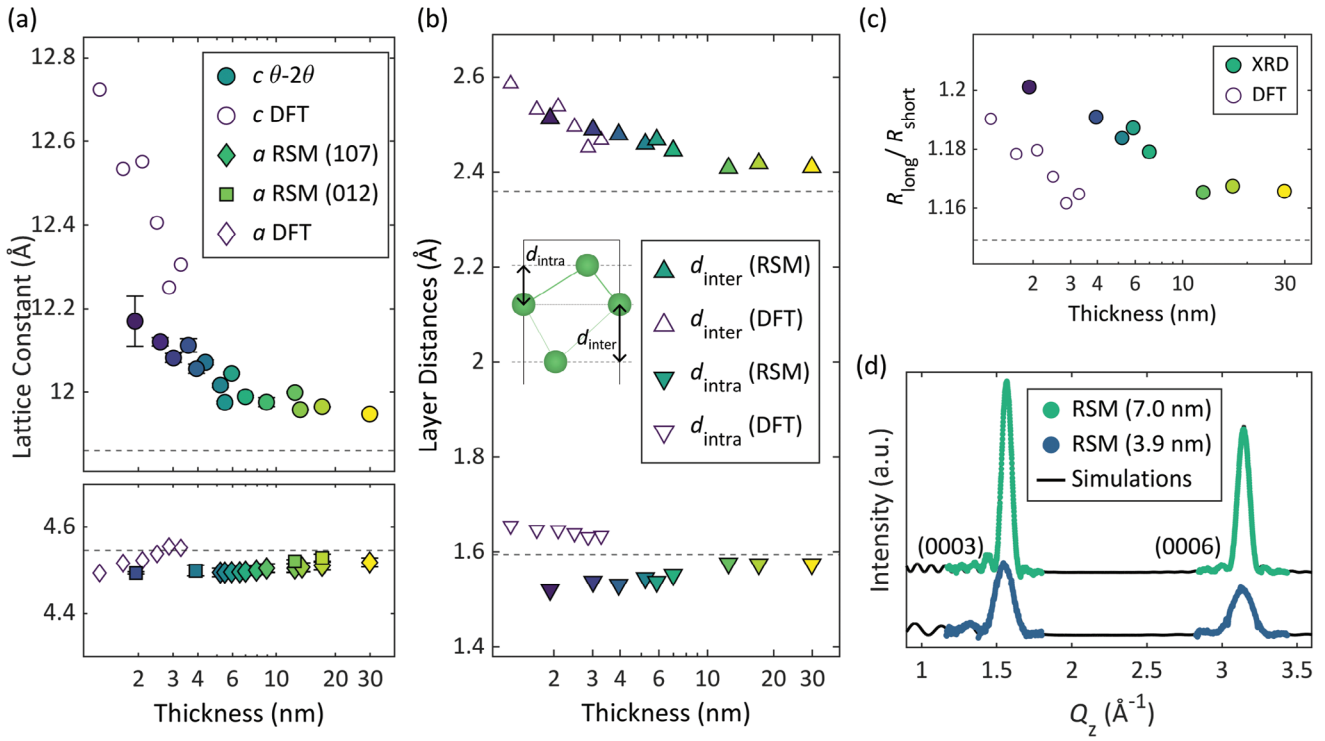

Figure 4. a) In-plane lattice constant a and out-of-plane lattice constant c for different film thicknesses determined by XRD analysis. The ultrathin films show a clear increase in the *c*lattice constant up to 2% over a thickness range of 30 nm, while *a* decreases by roughly 1%. Reference bulk data is shown as the horizontal dashed lines.[34] DFT calculations for free-standing slabs are shown as open circles and diamonds. b) The layer distances are illustrated with downward-pointing filled triangles for d_{intra} and upward-pointing filled triangles for d_{inter}. DFT calculations are shown as open triangles. The methods consistently indicate that the inter-bilayer distances increase. The inset is a depiction of half a unit cell – when viewed along the *a*-direction – and the defined inter- and intra-bilayer distances. c) Resulting Peierls distortion defined as the ratio of long to short bonds R_{long}/R_{short} within the unit cell. A strong increase in the distortion motif toward thinner films is clearly visible. d) The determination of inter- and intra-bilayer distances involves comparing the measured data with a simulation of the distorted unit cell. As can be observed, the simulations are in good agreement with the data.

A_{1g} phonon mode (circles). Specifically, the frequency of the A_{1g} mode in the thinnest layer increases by 5% compared to that in the thickest layer. Uncertainties on the phonon frequencies result from the Lorentzian curve fitting for Raman spectroscopy and from the damped harmonic oscillator and additional ZFE fitting for pump-probe spectroscopy. For the sake of clarity, error bars are not included if their size is smaller than the markers displayed. To our knowledge, such agreement between measurement results from Raman spectroscopy and optical fs pump-probe spectroscopy with ZFE has not been reported before. The significant blueshift of the phonon frequencies for reduced film thicknesses is qualitatively validated by density functional theory (DFT) calculations. More details on those calculations can be found in the supporting information.

2.4. Investigation of the Atomic Arrangement and the Peierls Distortion

Based on the pronounced blueshifts observed in the frequencies of the two phonon modes, it is reasonable to infer that the atomic arrangement within the trigonal phase undergoes clear changes as the film thickness decreases. For further examination, we revisit the results depicted in Figure 1. The diffraction peaks in the θ–2θ diffractograms shift to smaller Q_z values, i.e., to higher lattice constants, with decreasing thickness. The dashed gray lines marking the peak positions of the 29.9 nm film serve to emphasize the shift in the out-of-plane lattice constant. This shift is a direct consequence of a change of atomic arrangement with film thickness and is also well visible in the different Q_z values of the RSMs.

The dependence of the in-plane and out-of-plane lattice constants on film thickness is illustrated in **Figure** 4a. The lattice constants for the thickest sample slightly deviate from the established literature values for trigonal bulk phase of bismuth (a = 4.55 Å and c = 11.86 Å, denoted by the horizontal dashed lines).[34] The c lattice constant deviates upward by about half a percent, while the a lattice constant deviates downward by half a percent. Previous studies have demonstrated that thermal treatment can induce similar variations in the bulk lattice constants.[35] It is noteworthy that the c-lattice constant of the bismuth films converges toward the bulk value at even thicker film thicknesses (see Figure S13, Supporting Information). The values for thinner samples change gradually, so that the c lattice constant for the thinnest sample shows an increase of 2% compared to the thickest sample. This represents a significant change in unit cell height, which is particularly noteworthy because it doesn't occur abruptly. The lattice parameter already shows a growing deviation from the bulk value in the 10–20 nm thickness range. As the film thickness decreases further, the magnitude of

this effect also increases. At the same time, the reduction of the in-plane lattice constant a is less pronounced, with a change of 1% compared to the value of the thickest film.

While the c lattice constant in the ultrathin film regime increases from 11.97 to 12.17 Å, the a lattice constant changes are less pronounced below 5 nm.

One potential explanation for the observed trends is the adjustment of the bismuth in-plane lattice constant to the template on which it is grown, thereby minimizing lattice mismatch. However, our findings are incompatible with this hypothesis. A strain-induced tetragonal distortion of the lattice would suggest a coupled change of the in-plane and out-of-plane lattice constants. However, since the change in the out-of-plane lattice constant is significantly larger than that in the in-plane direction, an alternative explanation for the observed change in the out-of-plane lattice constant must be sought. Further, the TEM analysis reveals an incoherent interface between the passivation layer and the Bi film, which demonstrates a very weak coupling between film and substrate. Moreover, there are no indications of misfit dislocations, which would be expected to occur for the 18% misfit between Si and Bi in the presence of compressive strain. There is no evidence of a gradient in the in-plane lattice constant, which would suggest that it is smaller in proximity of the substrate and then increases gradually toward the center of the film.

Furthermore, the absence of a strain effect is corroborated by the distinct domain orientations observed. As illustrated in Figure S4 (Supporting Information) and detailed in Section 2.1, the majority of grains are oriented in the $(1\bar{1}00)$ direction and its twin domain. However, rotational domains are also present at φ = 27.5 ° and 30 °, and a residual fiber texture is observed. These grains all exhibit the same in-plane lattice constant. In contrast, for a strained film, we would expect to observe different lattice constants for the different rotations, due to the differing coincidence points with the substrate lattice.

Given these observations, we conclude that compressive strain from silicon substrates cannot explain the behavior seen in bismuth films studied here. Instead, we attribute it to a thickness-dependent equilibrium position of atoms and an evolving energy landscape. For the thickest films, the remaining discrepancies between the measured and literature values of the lattice constants can be attributed to the (weak) interaction between the film and the substrate.

In the following step, we assess the changes in atomic layer positions within the unit cell. To do this, we focus on the intensity ratios of the diffraction peaks. This intensity ratio is governed by the inherent trigonal distortion pattern. The unit cell exhibits a deviation from the cubic high-symmetry structure, resulting in the formation of bilayers. This phenomenon is known as Peierls distortion and sometimes denoted as the pairing of hexagonal planes.[36,37] To quantify the Peierls distortion the bond length ratio (R_{long}/R_{short}) is used. For large values of Peierls distortion of 1.2 and more typical covalent semiconductor behavior is expected, while values below are connotated with metavalent behavior.[38,39] The ratio can be calculated with the distance within a bilayer d_{intra}, the distance between the bilayers $d_{inter,}$ and the a lattice constant, as shown in Figure S14 (Supporting Information).

To investigate the atomic layer spacings and their evolution with decreasing film thickness, kinematic scattering theory, in conjunction with RSMs, proves to be a valuable approach.[40] Variations of the Peierls distortion within the unit cell induce changes in the structure factor and consequently affect the peak intensities observed in the measurements. In the cubic arrangement, the (0003) peak is forbidden due to destructive interference. An increasing Peierls distortion will lead to a gradual increase of the (0003) intensity, while the (0006) peak intensity decreases. Therefore, measuring the intensity ratio of both peaks and comparing it to simulations is a suitable method to obtain interplanar distances.

In order to determine a 1D profile of the totally scattered intensity the measured RSMs are integrated over the measured angles, including a background subtraction. The comparison of the integrated RSMs and the corresponding simulation is shown exemplarily for two film thicknesses in Figure 4d. This analysis allows the determination of the corresponding inter- and intra-bilayer distances for each film thickness, as depicted in Figure 4b. The comparison of experimental data and simulations reveals a clear trend in thickness: The inter-bilayer distances d_{inter} increase significantly as the films reach their minimum thickness, while the intra-bilayer distances d_{intra} show a slight decrease.

Figure 4c shows the Peierls distortion in the bismuth films as a function of film thickness. It can be seen that this parameter adequately reflects the increase of the distortion pattern toward thin films. It is noteworthy that bismuth is situated in a region of Peierls distortion, which is commonly associated with the bonding mechanism of metavalent bonding, an aspect that will be discussed in more detail in the following (Section 2.5).[38] This distortion is observed to be more pronounced in the thinnest sample, indicating a clear shift toward the covalent bond boundary.[39] The values in terms of fractional lattice spacings are provided in the Supporting Information.

The experimental results are compared to those obtained from DFT calculations of free-standing slabs with varying thicknesses. Similarly, an increase in the c lattice constant is observed for these slabs, which appears to be even more pronounced than in the experimental data. The discrepancies observed may be attributed to differences in the modeling approaches employed between XRD and DFT. A semi-empirical van der Waals correction has been applied, whereas the XRD is constrained to averages. The intra- and interlayer distances as a function of layer index are presented in the supporting information. In general, the surface layer exhibits greater distortion than the other layers, yet the inner part also differs from the bulk. With regard to the a lattice constant, a slight and gradual decrease is observed as the slabs become ultrathin. In comparison to the extent of the alterations in the out-of-plane lattice constant, these changes are relatively minor. To further investigate the impact of the absence of the Si substrate in the simulations, a series of calculations that also consider the Si substrate were conducted. As illustrated in Figure S15 (Supporting Information), the incorporation of the Si substrate in the simulation results in a reduction in the effect strength, while the trends remain.

In summary, the c lattice constant of the unit cell as well as the Peierls distortion increases for the ultrathin films. In addition, DFT calculations confirm the trends of these results. The DFT results, shown as open markers in Figure 4, are consistent with the observed trends of increasing Peierls distortion with decreasing film thickness. The observed discrepancy can be attributed to

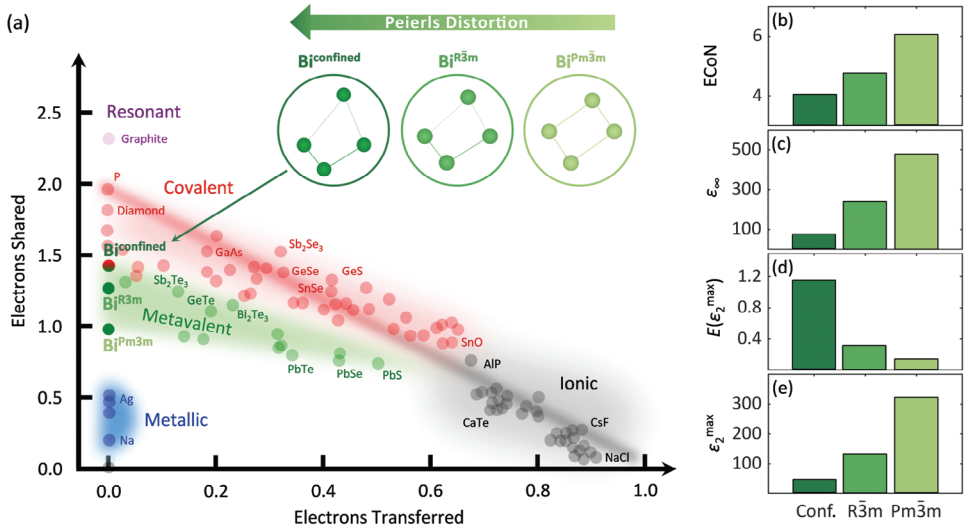

Figure 5. Relationship between atomic structure, chemical bonding, and physical properties through an analysis of quantum chemical bonding. a) A map that separates distinct bonding mechanisms based on the transfer and sharing of electrons between adjacent atoms. The green area of the map covers the bismuth phases, where bonding is characterized by an interplay between localization and delocalization. The cubic high-symmetry phase leans toward greater electron delocalization (more metallic), while the thin films tend toward enhanced electron localization (more covalent) with decreasing film thickness. In the upper right corner schematic representations of the analyzed bismuth structures, including the cubic Pm$\bar{3}$m, the trigonal R$\bar{3}$m in bulk, and a phase matching the distortion of the ultrathin films are shown. On the right side, a comparison is presented for four different properties calculated for the three bismuth phases: b) effective coordination number (*ECoN*), c) optical dielectric constant (ε_∞), d) energy of the absorption peak ($E(\varepsilon_2{}^{max})$), and e) the corresponding absorption strength ($\varepsilon_2{}^{max}$).

the elevated intralayer distances observed in the calculated structures. This results in a larger *c* lattice constant and a smaller Peierls distortion.

2.5. Quantum Chemical Bonding Analysis

Metavalent-bonded materials are characterized by a special competition between the tendency to delocalize electrons (metallic bonding) and the tendency to localize electrons (covalent bonding). The limited magnitude of the Peierls distortion in solids like GeTe and Sb_2Te_3, as well as Bi are indicative for this competition. Reducing the film thickness automatically changes the balance between both trends as has already been shown for GeTe and Sb_2Te_3.[41,42] It is tempting to speculate that the same mechanism is at play in Bi films. To confirm or refute this hypothesis, quantum chemical bonding descriptors can be employed.

Two key descriptors, the number of electrons transferred (ET) and the number of electrons shared (ES), serve as independent indicators of bonding. The atomic lattice is divided into non-overlapping domains (Bader basins) and the electron density is integrated over these domains to determine the domain population, which yields the relative number of electrons transferred after division by the formal oxidation state. Additionally, the delocalization index (DI), which represents the number of shared electron pairs between adjacent atoms, can be calculated by utilizing the two-electron density. By mapping these descriptors, known bonding mechanisms can be effectively categorized. The introduction of a certain property as the third dimension demonstrates the potential for designing specific material properties.[43]

Figure 5 shows the interplay of atomic arrangement, chemical bonding, and the resulting properties. The map spanned by the two bond descriptors is shown in Figure 5a. The structural motifs examined, illustrated in the upper right corner, show zero ET, as typical for monoatomic materials. With an ES value range between 1 and 1.5, the material exhibits metavalent bonding, resulting from the interplay of electron localization and delocalization. In the virtual cubic phase, linear chains of p-orbitals form throughout the material, embodying the ideal metavalent bonding with approximately one electron (half an electron-pair) shared between two atoms. The Peierls distortion in bulk bismuth reduces the p-orbital overlap, elevating the effective coordination number (*ECoN*) averaged ES value.[44] This averaging illustrates that while the total ES value remains constant, the electrons progressively shift toward the shorter bond and consequently into the bilayer as the distortion increases. In addition, the ES values of short and long bonds for center and surface are compared in the supporting information. Reducing the film thickness further amplifies the distortion, increasing ES as the p-orbital overlap decreases. Preliminary indications of this phenomenon have already appeared in the literature, where the behavior of bismuth layers is characterized as "semicovalent".[25]

To further substantiate the occurrence of metavalent bonding in bismuth, recent experimental findings reveal that elemental bismuth displays an unusual chemical bond rupture, a phenomenon explored with atom probe tomography (APT), with a specific focus on laser-assisted field emission.[45] This investigation considers two processes: the probability of molecular ions (PMI), indicating the likelihood of molecular ions evaporation over single (atomic) ions, and the probability of multiple events (PME), which refers to the correlated field-evaporation of more than one fragment upon laser- or voltage pulse excitation. Notably, bismuth demonstrates a bond breakage comparable

to mono- and sesquichalcogenides. Consequently, the study suggests the presence of the same unconventional bonding mechanism in bismuth as in these chalcogenides, which is metavalent bonding.[45]

The three cases depicted on the material map (virtual cubic $Pm\bar{3}m$, bulk trigonal $R\bar{3}m$ and a $R\bar{3}m$ phase matching the distortion of the ultrathin films) can be systematically analyzed in terms of their properties using DFT. This allows us to determine whether the changes in optical properties are due to the increasing distortion and the associated changes in chemical bonding. The right side of Figure 5b–e shows four properties: the effective coordination number (*ECoN*), the optical dielectric constant (ε_∞), the maximum absorption strength (ε_2^{max}), and the corresponding photon energy ($E(\varepsilon_2^{max})$). The reduction of the *ECoN* from 6 to 4 with increasing Peierls distortion suggests a change from a perfectly octahedral to a defective or distorted octahedral bonding environment. Notably, the measured trends in the optical dielectric constant, absorption strength, and associated energy (as shown in Figure 2) are observed to be replicated by the calculations. When the distortion is completely removed (cubic phase), the trend persists even further. This highlights the significant dependence of the optical properties of bismuth on the degree of Peierls distortion.

3. Discussion

Thin bismuth films have been shown to display pronounced changes of their properties with decreasing film thickness from the bulk limit to 1.9 nm thin films. A reduction in the optical dielectric constant and the height of the absorption maximum is observed with a decrease in layer thickness. Concomitantly, the absorption peak undergoes a shift toward higher photon energies. Both phonon modes, the in-plane E_g mode, and the out-of-plane A_{1g} mode, exhibit a blue shift for thinner films. This effect is more pronounced for the in-plane E_g mode. Additionally, the unit cell volume increases for the thinnest films, while the inter-bilayer distance increases and the intra-bilayer distance decreases. This results in a more pronounced Peierls distortion for the ultra-thin films.

These pronounced property changes are not seen in typical elemental semiconductors like Si or Ge. In Bi films, these changes are linked to significant changes in bonding, i.e., a bond confinement effect. As thickness decreases, systematic bonding changes lead to increased Peierls distortion and atomic volume. This behavior is a unique characteristic of metavalent bonding, where electron localization competes with delocalization, as reflected in their room-temperature electrical conductivity.[44,45] Depending on the film thickness, electron localization, and delocalization are adjusted to achieve the corresponding energy minimum by altering the atomic equilibrium position. This behavior is well documented for thin GeTe layers.[46] This can also be described in terms of the layer thickness dependence of the cohesive energy per atom.[40] It is important to note that the observed effect is not strain related. It is also significantly larger than would be expected from surface or interface effects alone. The aforementioned metavalent composites GeTe and SnTe have already been shown to exhibit these properties by means of DFT calculations, where the structure of thin films of these materials shows significant deviations from the bulk phases, even at thicknesses exceeding 18 bilayers.[47] This phenomenon is also observed in the Bi thin films of this study.

The bond confinement results in variations in optical and vibrational properties. The localization of electrons within the bilayers results in fewer electrons between them, reducing interlayer coupling and causing the unit cell to expand out-of-plane. While crystal symmetry remains unchanged, this expansion increases distortion motifs while simultaneously enhancing coupling strength within the bilayers—in-plane direction—evidenced by a substantial increase in phonon mode frequency. Consequently, since the out-of-plane phonon mode must counteract this increased coupling, a higher restoring force leads to an elevated mode frequency in the out-of-plane direction as well.

In addition to its strong influence on the phonon band structure, Peierls distortion also affects the electronic band structure. This influence is evident when the optical properties are examined in addition to the quantum chemical bonding analysis. The half-filled outer p-orbital in the electron configuration of bismuth indicates that the electronic band structure near the Fermi energy is dominated by the overlap of these p-orbitals. As the structural distortion increases and deviates further from the cubic high symmetry phase, the directional, chain-like p-orbital overlap decreases. The resulting change in band structure is reflected in the density of states and correlated absorption behavior of the material, as depicted in **Figure 6**. The majority of the occupied states below the Fermi level and most of the unoccupied states above the Fermi level originate from the p-orbitals. Therefore, the optical transitions that contribute to the maximum of the imaginary part of the dielectric function are primarily p-to-p orbital transitions.

While examining the phonons in real-time, we uncovered an additional effect related to film thickness. Previously, the increasing redshift of the A_{1g} mode frequency with excitation intensity toward thin films could be attributed to the higher density of excited charge carriers present in thin films.[48] However, we have observed that this trend only persists up to 3.5 nm. Beyond this thickness, a contrary trend emerges. The amplitude ratio of the two modes in the Raman shifts changes within the same range of film thickness. Additionally, the in-plane mode becomes undetectable in anisotropic EO sampling. This indicates that in these ultra-thin films, the excess energy from carrier excitation is initially mainly converted into the excitation of the out-of-plane mode, while the in-plane mode is less favored. In addition, we have succeeded in resolving the superimposed redshift and blueshift of the phonon frequencies using the simple method of ZFE. This shows that the displacive excitation of coherent phonons (DECP) model for minimal atomic displacements is consistent with the Raman scattering process, wherein atoms oscillate around their initial lattice positions. This discovery facilitates the analysis of superimposed effects in ultrafast transient reflection measurements. For even thinner layers (three and four bilayers), a comparable blue shift of the E_g mode was reported, while the A_{1g} phonon peak exhibited a splitting and underwent a red shift in comparison to the bulk.[19]

These findings showcase the significance of film thickness as a tunable parameter in the modulation of properties in pnictogens. This is relevant for the advancement of functional

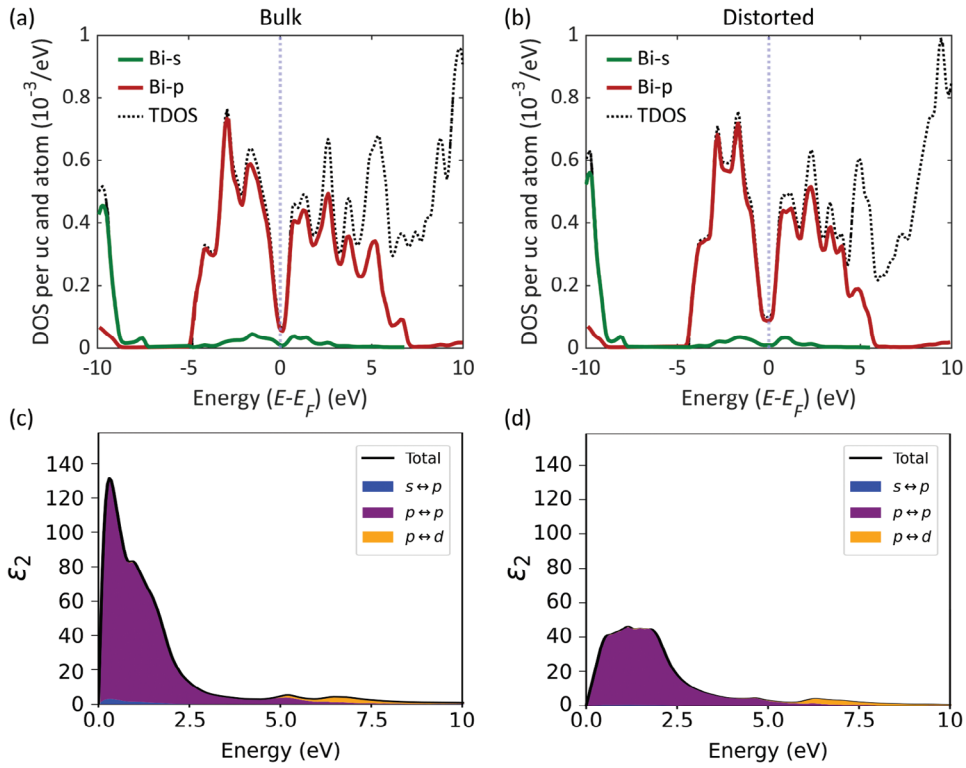

Figure 6. Density of states (DOS) per unit cell and atom for a) the bulk phase and b) the phase matching the distortion of the ultrathin films. The DOS of the bulk phase shows a slightly broader p-orbital contribution, indicating greater electron delocalization. In the distorted case, bond confinement leads to increased electron localization and a narrower band. Orbital resolved imaginary part of the dielectric functions of c) the bulk phase and of d) the phase matching the distortion of the ultrathin films. The optical properties are driven by the p–p transitions, shown in purple.

materials, broadening the scope of their potential applications. In recent years, the application landscape of chalcogenides has experienced a notable transformation. Historically employed predominantly as media for optical or electrical data storage,[49] their utilization has now evolved toward optical components within photonic circuits.[50,51] This evolution is particularly evident in their adoption for neuromorphic computing and photonic phase-change memory applications.[52,53] Notably, these applications require new performance requirements, in terms of switching speed, band gap between material phases, and associated optical characteristics such as contrast and absorption losses.[38] Responding to the altered requirements of these applications, chalcogenide materials are also evolving, i.e., toward compounds with higher sulfur or selenium content.[54] Selenium or sulfur-based chalcogenides can be used directly,[55] or the tellurium can be substituted with sulfur or selenium in prominent alloys such as GeSbTe (GST).[56]

In order to avoid a complication of the material systems used, the approach of drastically reducing the film thickness is highly interesting and is used in heterostructure devices.[57] In addition to the promising properties of the crystalline phase, it is possible to stabilize amorphous phases in ultra-thin films, which are too unstable for use in bulk at room temperature. This behavior could be shown for a device working with Sb_2Te_3[58] as well as in pure antimony,[59,60] so that in addition to the chalcogenides, the pnictogens also show considerable phase change material (PCM) application potential at low layer thicknesses.

4. Conclusion

In summary, a study of the impact of thickness upon film properties in thin bismuth films has been performed. Significant changes of properties upon reducing the film thickness have been identified. A decrease in the optical dielectric constant and the height of the absorption maximum is noted. Simultaneously, the absorption peak shifts to higher photon energies. Additionally, both phonon modes, the in-plane E_g mode, and the out-of-plane A_{1g} mode, show a blue shift. The property changes are also mirrored in changes of atomic arrangement. For the thinnest films, the unit cell volume increases, the interbilayer distance grows, and the intrabilayer distance decreases, leading to a more pronounced Peierls distortion. This phenomenon can be attributed to the metavalent bonding in bismuth. The bond confinement in ultrathin films influences the competition between electron localization and delocalization, causing electrons to localize within the bilayers. This demonstrates that property design by film thickness is feasible not only in chalcogenides but also in monoatomic pnictogens.

5. Experimental Section

Sample Preparation: The substrate preparation involved cutting 4-inch Si (111) wafers with a resistivity exceeding 5000 ohm cm and a miscut angle of 0.05 ° into 10 mm x 10 mm pieces. Each substrate piece underwent chemical cleaning using Piranha 1:1 solution, a mixture of 37% hydrogen

peroxide (H_2O_2) and 96% sulfuric acid (H_2SO_4), for 10 min, followed by rinsing with de-ionized water for 15 min. Prior to loading into the MBE chamber, the Si (111) surface's native oxide was etched using a 1% HF solution for 5 min and subsequently rinsed with de-ionized water to ensure saturation of dangling bonds with H atoms.

The epitaxial growth occurred in an ultra-high vacuum MBE chamber with a base pressure of 1×10^{-10} mbar, increasing to $\approx 5 \times 10^{-10}$ mbar during growth. Before the epitaxy of Bi thin films, hydrogen atoms that saturate Si dangling bonds were removed by annealing the substrates at a maximum temperature of 600 °C. The selection of annealing temperature was crucial as it ensured the emergence of natural 1×1 Si surfaces while inhibiting higher-order reconstructions such as $\sqrt{3} \times \sqrt{3}$ and 7×7, which required higher temperatures. The removal of hydrogen atoms revealed Si dangling bonds on the 1×1 surfaces, which, upon exposure to the Bi beam flux, saturate and assemble into $\sqrt{3} \times \sqrt{3}$– Bi reconstruction. To avoid this, the substrates were cooled to the growth temperature of 40 °C and thereafter subjected to the Bi beam flux to passivate the dangling bonds. The reduced temperatures prevent the reconstruction into $\sqrt{3} \times \sqrt{3}$– Bi terminations and yield stable 1×1 surfaces passivated by a monolayer of Bi atoms. These Bi-terminated 1×1 surfaces are the key to acquire high-quality, ultra-smoothm, and strain-free thin films of Bi, presented in this work.

To grow thin films, high-purity Bi (99.9999%) in the Knudsen cell was heated within the temperature range of 480–575 °C to stabilize the Bi flux and achieve the target growth rate (R_{TF}). The thin films were then grown for durations ranging from 10 to 90 min, depending on the applied R_{TF}. Bi as bulk exhibited the rhombohedral (trigonal) crystal structure. The Bi terminated 1×1 hexagonal surfaces facilitated the growth of Bi films in the trigonal phase. Moreover, Bi similar to Nb, crystallized at room temperature and that is why the optimum growth temperature (T_{sub}) was identified by Jalil et al. to be 40 °C for the trigonal phase (for details: refer to[23] Figure 2).

In contrast to Bi bulk crystals, Bi thin films exhibited a shift in orientation from (001) to (102) along the normal axis when subjected to temperatures above 50 °C. Upon further increase in temperature, it resulted in restructuring of the trigonal (102) phase into a non-layered orthorhombic phase (for details: refer to[23] Figure 5). The orthorhombic phase of Bi, unlike the trigonal one, exhibited significant strain in form of buckling, and therefore, the fully coalesced films could only be achieved up to a maximum thickness of 30 nm (for details: refer to[23] Figures 6-11). In short, Bi thin films could be achieved in either of the two desirable phases, namely trigonal or orthorhombic, with the target phase being accurately regulated by the growth parameters (T_{sub}, R_{TF}) and the substrate surface/termination. Using the Bi terminated 1×1 surfaces, the optimum growth of Bi thin films in the trigonal phase was achieved at (T_{sub}, R_{TF}) = (40 °C, 22 nm h^{-1}) whereas, the orthorhombic phase was realized at (T_{sub}, R_{TF}) = (100 °C, 32 nm h^{-1}). This work exclusively focused on the trigonal phase.

It should be noted that only ex situ characterization techniques were used to assess the crystalline phase after growth. It could not be determined with certainty whether the growth occured directly in the trigonal (001) orientation or whether a phase transition occured upon reaching a critical thickness. This research question would undoubtedly merit further investigation, but was beyond the scope of this paper. Nevertheless, TEM and XRD studies confirmed that these resulting films were unambiguously pure trigonal (001). For further optimization details, please refer to Jalil et al. where extensive optimization parameters were discussed.[23]

After epitaxy, the samples were capped with ≈10 nm thick Al_2O_3.

Scanning Electron Microscopy: SEM was performed via "Leo 1550 ZAT" setup using an acceleration voltage between 2 and 5 keV, which provided the information about the surface texture.

Femtosecond Pump Probe Reflectivity: Ultrafast optical measurements were conducted using a standard reflection-type, two-color pump-probe experiment in both isotropic and anisotropic (electro-optic sampling) configurations. The 800 nm wavelength, 80 fs width pump beam was separated from a Ti:Sapphire regenerative femtosecond amplifier, chopped at 1500 Hz, and directed to a free-standing optical delay line before being focused on the sample to a spot size of 100 µm in diameter. The probe pulses were frequency converted to 520 nm via sum frequency generation in an optical parametric amplifier and focused to a 30 µm diameter spot on the sample. The detection unit comprised two balanced Si photodiodes connected to variable gain current amplifiers and a data acquisition card. All measurements were taken at pump fluences between 0.1 and 1 mJ cm^{-2}, with the probe fluence being ten times lower. To eliminate systematic errors on laboratory time scales, the order of data point recording and the positioning of the delay line were randomized. The anisotropic transient reflectance was calculated from the s- and p-polarized components of the reflected light using the electro-optic detection scheme: $\Delta R_{EO} = \frac{\Delta(R_s - R_p)}{R_0}$, while the isotropic transient reflectance was calculated from the whole signal: $\Delta R = \frac{\Delta(R_s + R_p)}{R_0}$. A polarizing beam splitter cube was used to split the reflected probe beam correspondingly. Both, isotropic and anisotropic transient reflectance was normalized to the steady state reflectance R_0. Reversibility of optical excitation was ensured by monitoring the static reflectivity gained for the probe-pulse when the pump-pulse was chopped.

Raman Spectroscopy: Raman spectroscopy measurements were conducted with a commercial WITec system (alpha300), operating in backscattering geometry. A diode pumped solid state laser supplied linearly polarized light with a wavelength of 531 nm (2.33 eV). This was delivered through a single-mode optical fiber and used to excite the sample. The spot size of 400–500 nm was obtained by employing a long working focusing lens with a numerical aperture of 0.70. By setting the excitation power to 500 µW, significant heating effects were avoided. For detection, the reflected light was delivered through a single-mode optical fiber to a charge coupled spectrometer with a grating of 2400 lines per mm. All measurements were obtained at room temperature with a 50× (NA = 0.7) objective, with a resolution close to the diffraction limit (≈800 nm).

X-Ray Reflection and Diffraction: The measurements were measured parallel on a "Rigaku Smartlab" system with a rotating anode and a Bruker D8 Discover with a classical X-ray tube both employing a Cu Kα1 radiation source (λ = 1.540562 Å)), selected by a Ge (220) 2 bounce monochromator. Reciprocal space maps on the Rigaku system were measured with the detector in 1D mode, while measurements on the Bruker system were measured with a 0D detector. For θ-2θ and (003n) symmetric /(017) asymmetric Reciprocal space maps, the peak area was confined with slits (1 and 0.6 mm), while a 1 mm snout collimator was used for the Phi scans and (01n2n) symmetric RSMS. For the evaluation of the out of plane lattice constants the θ-2θ scans of the (003n) peaks were fitted individually and the lattice constant was obtained from a linear fit of the peak positions. For the in-plane lattice constant, the (0n2n) peaks were measured and fitted for different sample rotations and the resulting lattice constant was averaged. The evaluation of distortion was performed on the (003n) peak series, with the details of the simulation in the Supporting Information.

Electron Backscatter Diffraction: The orientation and size of the thin film grains were investigated using electron backscatter diffraction (EBSD). Prior to the measurements, the samples were subjected to a 20 s immersion in a 1% hydrofluoric acid solution to remove the Al_2O_3 capping. The EBSD system (AMETEK, NJ, USA) was incorporated into the FEI Helios 650 NanoLab system. The scanning electron microscope (SEM) was typically operated with an acceleration voltage of 10–15 keV and a beam current of 3.2 nA, with a chamber pressure of $\approx 10^{-6}$ mbar. The sample tilt and working distance were set to 70° and 13 mm, respectively. With these parameters, the EBSD lateral resolution was ≈30 nm, and the typical exposure frame rates for the EBSD camera were ≈20 to 40 fps. Subsequent to data acquisition, the data were treated with a grain dilation algorithm using TSL OIM Analysis.

Transmission Electron Microscopy: The lamellae for TEM were prepared by a focused ion beam (FIB) system "FEI Helios Nanolab 600i". Before cutting with the Ga ions in FIB, Pt layers were deposited on the sample surface to protect the specimen from damaging. Plasma cleaning was carried out to remove any surface contamination of the lamella before inserting into the microscope. Scanning transmission electron microscopy (STEM) was performed with "FEI Titan G2 80–200 ChemiSTEM" microscope, which was equipped with a spherical aberration probe "Cs" corrector and the

annular dark-field detectors. High-angular annular dark-field (HAADF) and Bright filed (BF) images were acquired at 200 kV.

Optical Spectroscopy: Ellipsometry spectra were measured using three angles of incidence (65°, 70°, and 75°) on a J.A.Woollam M-2000UI spectroscopic ellipsometer. The deuterium and halogen lamps served as the sources of illumination for the setup. A silicon CCD camera detected visible and ultraviolet light, while an InGaAs diode array captured lower energy photons. In total, 584 channels with an average of 7 meV resolution over 0.72 to 5.14 eV were available.

Normal incidence reflectance data were collected by fiber grating in the range from 9100 to 45 000 cm^{-1} with an Avantes AvaSpec-ULS2048CL-EVO with the use of a CMOS linear image sensor. Deuterium and halogen lamps (AvaLight-DH-S-BAL) were used as illumination sources. An aluminum mirror served as reference.

Reflectance measurements in the 200 respectively 500 to 16 000 cm^{-1} range were performed on a Bruker Vertex 80v Fourier-transform infrared spectrometer (FTIR). A 200 nm thick silver mirror served as a reference. Multiple source (Hg-arc, globar, and tungsten lamp), beam splitter (Mylar 50 µm, multilayer, KBr, and CaF2), and detector (DLaTGS (one with polyethylene and one with KBr window), liquid nitrogen-cooled InSb and room-temperature Si photodiode) combinations were utilized to cover the entire spectral range.

The dielectric functions of the samples were determined using a three-layer model (capping/thin film/substrate) within the J.A. Woollam CompleteEASE software. A Levenberg-Marquardt regression algorithm was employed for parameter optimization. The process began with the measurement and analysis of the bare substrate to extract its dielectric function. Subsequently, the dielectric function of the capping layer was determined based on measurements of the substrate with the capping layer alone. In the next step, the dielectric functions of the substrate and capping layer were kept fixed, and the dielectric properties of the bismuth thin films were extracted, using the film thicknesses determined via XRR. Due to higher roughness, for the three thickest samples an additional layer between capping and thin film was introduced. For this layer, an effective medium approach (EMA) with use of the Bruggeman model was fitted. The dielectric function of the bismuth thin films was described by employing a summation of a constant dielectric background along with Tauc-Lorentz oscillators and a Drude contribution. All the parameters were fitted to convergence.

Density Functional Theory (DFT) Studies: To validate the experimental observations, density functional theory (DFT) simulations were conducted utilizing the PBE-GGA (Generalized Gradient Approximation by Perdew, Burke, and Ernzerhof)[61] functional in conjunction with PAW (projector augmented wave) and norm-conserving (NC) pseudo-potentials, as implemented in VASP and ABINIT.[62–65] For ES/ET calculations using Abinit 7.10.5 and DGRID 4.7, k-point grids ranging between 5 × 5 × 3 and 10 × 10 × 10 were used for the largest and smallest unit cells respectively. The energy cutoff was set to 25 Ha with a smearing of 0.005 Ha. For band structure calculations using Quantum ESPRESSO 6.8, k-point grids ranging between 24 × 24 ×9 and 30 × 30 × 30 were used for the largest and smallest unit cells respectively. The energy cutoff was set to 100 Ry with a smearing of 0.015 Ry. For dielectric function calculations using Quantum VASP 5.4.4, k-point grids ranging between 24 × 24 × 9 and 30 × 30 × 30 were used for the largest and smallest unit cells respectively. The energy cutoff was set to 550 eV with a smearing of 0.1 eV.

The calculation of the A_{1g} and E_g phonon frequencies was performed using Quantum Espresso.[66] In general, a norm-conserving pseudopotential (NC) was employed, coupled with a PBE functional and a vdW-Grimme-D2 correction.[67] Initially, the bulk system was relaxed using the "vc-relax" calculation in QE, yielding a lattice parameter of a = 4.465 Å, which deviates by 1.8% from the measured reference value of a = 4.546 Å. Subsequently, the "a" parameter obtained from vc-relax was applied to all slab systems (1BL-2BL-3BL-4BL-6BL-7BL-8BL-9BL-12BL), and for each of these systems, a relaxation was performed along the z-direction only ("vc-relax" calculation + cell_dofree = "z" in QE). The choice of a fixed "a" parameter for different thicknesses ensured that the parameter space used was not too large. This was justified by the fact that the change in the *a* lattice constant was significantly smaller than the change in the c lattice constant. The slabs were simulated by constructing supercells with 15 Å of vacuum above and below the system to suppress any vertical interactions arising from the application of periodic boundary conditions. For the relaxation of all simulated systems, an 8 × 8 × 1 Monkhorst-Pack k-mesh was chosen, along with a kinetic energy cutoff for wavefunctions set to 80 Ry ("ecutwfc" in QE). Concerning the calculation of phonon frequencies, the ph.x code within QE was utilized. This code implemented density functional perturbation theory (DFPT), enabling calculations at the Gamma-point without the need to construct large supercells in any direction.

Supporting Information

Supporting Information is available from the Wiley Online Library or from the author.

Acknowledgements

F.H., T.V., T.S., and M.W. acknowledge financial support from NeuroSys as part of the initiative "Clusters4Future", which is funded by the Federal Ministry of Education and Research BMBF (03ZU1106BA). R.M. gratefully acknowledges funding from the PRIN 2020 project "Neuromorphic devices based on chalcogenide heterostructures" funded by the Italian Ministry for University and Research (MUR). The authors gratefully acknowledge the computational the computing time provided to them at the NHR Center NHR4CES at RWTH Aachen University (project number p0020357) and at Cineca Supercomputing Center (project CN HPC 1464877 – MultiPCM). K.G. Wirth from the Institute of Physics (IA) of RWTH Aachen University is greatly acknowledged for helpful discussions. C. Ringkamp is greatly acknowledged for additional sample growth and XRD measurements.

Open access funding enabled and organized by Projekt DEAL.

Conflict of Interest

The authors declare no conflict of interest.

Author Contributions

F.H. and P.K. contributed equally to the work. F.H. initiated the project. M.W. supervised the project. A.R.J. fabricated the samples and performed XRD, XRR, TEM, and SEM measurements, and analyzed them regarding film thickness. P.K. carried out advanced XRD analyses to determine the c and a lattice constants and the layer spacings and provided important suggestions and discussions on the manuscript. J.K. carried out EBSD measurements. L.B. had carried out XRD measurements. T.S. conducted optical spectroscopy measurements and data analysis. T.V., J.F., and F.H. performed pump-probe and Raman measurements and analyzed the data. J.M. helped in the interpretation of the data. C-F.S. and D.K. calculated ES/ET values. C-F.S. calculated optical properties. Y.X. calculated structural properties. S.R. calculated phonon frequencies, dielectric functions of slabs, and structural properties of the super cell with Si and Bi. R.M. supervised these calculations. J.M. helped interpret the TEM data. F.H. prepared the figures and wrote the manuscript. M.W. significantly revised the manuscript. All authors commented on and approved the submission of this manuscript.

Data Availability Statement

The data that support the findings of this study are available from the corresponding author upon reasonable request.

Keywords

confinement, materials design, metavalent bonding, Peierls distortion, ultrathin films

Received: November 4, 2024
Revised: December 13, 2024
Published online:

[1] F. Ersan, D. Keçik, V. Özçelik, Y. Kadioglu, O. Ü. Aktürk, E. Durgun, E. Aktürk, S. Ciraci, *Appl. Phys. Rev.* **2019**, *6*, 023108.
[2] F. Reis, G. Li, L. Dudy, M. Bauernfeind, S. Glass, W. Hanke, R. Thomale, J. Schäfer, R. Claessen, *Science* **2017**, *357*, 287.
[3] J. Gou, H. Bai, X. Zhang, Y. L. Huang, S. Duan, A. Ariando, S. A. Yang, L. Chen, Y. Lu, A. T. S. Wee, *Nature* **2023**, *617*, 67.
[4] S. Ghosal, S. Chowdhury, D. Jana, *ACS Appl. Mater. Interfaces* **2021**, *13*, 59092.
[5] L. Cheng, H. Liu, X. Tan, J. Zhang, J. Wei, H. Lv, J. Shi, X. Tang, *J. Phys. Chem. C.* **2014**, *118*, 904.
[6] L. Aggarwal, P. Zhu, T. L. Hughes, V. Madhavan, *Nat. Commun.* **2021**, *12*, 4420.
[7] I. K. Drozdov, A. Alexandradinata, S. Jeon, S. Nadj-Perge, H. Ji, R. Cava, B. A. Bernevig, A. Yazdani, *Nat. Phys.* **2014**, *10*, 664.
[8] C.-H. Hsu, X. Zhou, T.-R. Chang, Q. Ma, N. Gedik, A. Bansil, S.-Y. Xu, H. Lin, L. Fu, *Proc. Natl. Acad. Sci. U.S.A.* **2019**, *116*, 13255.
[9] O. Prakash, A. Kumar, A. Thamizhavel, S. Ramakrishnan, *Science* **2017**, *355*, 52.
[10] C. Wang, L. Wang, F. Li, F. Cheng, J. Chen, *Adv. Mater.* **2017**, *29*, 1702212.
[11] M. Yarema, M. V. Kovalenko, G.n. Hesser, D. V. Talapin, W. Heiss, *J. Am. Chem. Soc.* **2010**, *132*, 15158.
[12] M. Pumera, Z. Sofer, *Adv. Mater.* **2017**, *29*, 1605299.
[13] R. M. Kaloari, E. Widianto, I. Dana, A. Lukmantoro, T. Kato, S. Iwata, E. Suharyadi, M. Absor, A. Ulil, I. Santoso, *Thin Solid Films* **2023**, *773*, 139825.
[14] Y. F. Komnik, I. Berkutov, V. Andrievskıı, *Low Temp. Phys.* **2005**, *31*, 326.
[15] M. Hase, K. Mizoguchi, H. Harima, S.-i. Nakashima, K. Sakai, *Phys. Rev. B.* **1998**, *58*, 5448.
[16] M. Hase, K. Mizoguchi, H. Harima, S. Nakashima, M. Tani, K. Sakai, M. Hangyo, *Appl. Phys. Lett.* **1996**, *69*, 2474.
[17] M. Hase, M. Kitajima, S.-i. Nakashima, K. Mizoguchi, *Phys. Rev. Lett.* **2002**, *88*, 067401.
[18] D. M. Fritz, D. Reis, B. Adams, R. Akre, J. Arthur, C. Blome, P. Bucksbaum, A. L. Cavalieri, S. Engemann, S. Fahy, *Science* **2007**, *315*, 633.
[19] K. Ishioka, M. Kitajima, O. V. Misochko, T. Nagao, *Phys. Rev. B.* **2015**, *91*, 125431.
[20] G. Jnawali, D. Boschetto, L. Malard, T. Heinz, G. Sciaini, F. Thiemann, T. Payer, L. Kremeyer, F.-J. Meyer zu Heringdorf, M. Horn-von Hoegen, *Appl. Phys. Lett.* **2021**, *119*, 091601.
[21] F. Thiemann, G. Sciaini, A. Kassen, T. S. Lott, M. Horn-von Hoegen, *Phys. Rev. B.* **2024**, *109*, L041105.
[22] W. Huang, J. Zhu, M. Wang, L. Hu, Y. Tang, Y. Shu, Z. Xie, H. Zhang, *Adv. Funct. Mater.* **2021**, *31*, 2007584.
[23] A. R. Jalil, X. Hou, P. Schüffelgen, J. H. Bae, E. Neumann, G. Mussler, L. Plucinski, D. Grützmacher, *Nanomaterials* **2023**, *13*, 2143.
[24] A. R. Jalil, D. Grützmacher, PhD Thesis, RWTH Aachen University, Aachen, Germany **2022**.
[25] T. Nagao, J. Sadowski, M. Saito, S. Yaginuma, Y. Fujikawa, T. Kogure, T. Ohno, Y. Hasegawa, S. Hasegawa, T. Sakurai, *Phys. Rev. Lett.* **2004**, *93*, 105501.
[26] M. Kammler, M. Horn-von Hoegen, *Surf. Sci.* **2005**, *576*, 56.
[27] S. Yaginuma, T. Nagao, J. Sadowski, M. Saito, K. Nagaoka, Y. Fujikawa, T. Sakurai, T. Nakayama, *Surf. Sci.* **2007**, *601*, 3593.
[28] T. Nagao, T. Doi, T. Sekiguchi, S. Hasegawa, *Jpn. J. Appl. Phys.* **2000**, *39*, 4567.
[29] M. Wuttig, V. L. Deringer, X. Gonze, C. Bichara, J.-Y. Raty, *Adv. Mater.* **2018**, *30*, 1803777.
[30] M. Fox, *Optical Properties of Solids*, Vol. *3*, Oxford university Press, Oxford, England, **2010**.
[31] L. Guarneri, S. Jakobs, A. von Hoegen, S. Maier, M. Xu, M. Zhu, S. Wahl, C. Teichrib, Y. Zhou, O. Cojocaru-Mirédin, *Adv. Mater.* **2021**, *33*, 2102356.
[32] T. Dekorsy, T. Pfeifer, W. Kütt, H. Kurz, *Phys. Rev. B.* **1993**, *47*, 3842.
[33] J. Höhne, U. Wenning, H. Schulz, S. Hüfner, *Z. Phys. B.* **1977**, *27*, 297.
[34] P. Cucka, C. Barrett, *Acta Crystallogr.* **1962**, *15*, 865.
[35] M. Pilloni, G. Ennas, V. Cabras, V. Denotti, V. B. Kumar, A. Musinu, Z. Porat, A. Scano, A. Gedanken, *J. Therm. Anal. Calorim.* **2015**, *120*, 1543.
[36] K. J. Chang, M. L. Cohen, *Phys. Rev. B.* **1986**, *33*, 7371.
[37] R. E. Peierls, *Quantum Theory of Solids*, Clarendon Press, Oxford, UK **1996**.
[38] B. J. Kooi, M. Wuttig, *Adv. Mater.* **2020**, *32*, 1908302.
[39] J.-Y. Raty, M. Wuttig, *J. Phys. D: Appl. Phys.* **2020**, *53*, 234002.
[40] P. Kerres, R. Mazzarello, O. Cojocaru-Mirédin, M. Wuttig, *Phys. Status Solidi* **2024**, *221*, 2300921.
[41] J. Mertens, P. Kerres, Y. Xu, M. Raghuwanshi, D. Kim, C. F. Schön, J. Frank, F. Hoff, Y. Zhou, R. Mazzarello, *Adv. Funct. Mater.* **2024**, *34*, 2307681.
[42] P. Kerres, Y. Zhou, H. Vaishnav, M. Raghuwanshi, J. Wang, M. Häser, M. Pohlmann, Y. Cheng, C. F. Schön, T. Jansen, *Small* **2022**, *18*, 2201753.
[43] C.-F. Schön, S. van Bergerem, C. Mattes, A. Yadav, M. Grohe, L. Kobbelt, M. Wuttig, *Sci. Adv.* **2022**, *8*, eade0828.
[44] M. Wuttig, C. F. Schön, J. Lötfering, P. Golub, C. Gatti, J. Y. Raty, *Adv. Mater.* **2023**, *35*, 2208485.
[45] O. Cojocaru-Mirédin, Y. Yu, J. Köttgen, T. Ghosh, C. F. Schön, S. Han, C. Zhou, M. Zhu, M. Wuttig, *Adv. Mater.* **2024**, *36*, 2403046.
[46] R. Wang, W. Zhang, J. Momand, I. Ronneberger, J. E. Boschker, R. Mazzarello, B. J. Kooi, H. Riechert, M. Wuttig, R. Calarco, *NPG Asia Mater.* **2017**, *9*, e396.
[47] I. Ronneberger, Z. Zanolli, M. Wuttig, R. Mazzarello, *Adv. Mater.* **2020**, *32*, 2001033.
[48] F. Thiemann, G. Sciaini, A. Kassen, U. Hagemann, F. M. zu Heringdorf, M. Horn-von Hoegen, *Phys. Rev. B.* **2022**, *106*, 014315.
[49] M. Wuttig, N. Yamada, *Nat. Mater.* **2007**, *6*, 824.
[50] M. Wuttig, H. Bhaskaran, T. Taubner, *Nat. Photonics* **2017**, *11*, 465.
[51] C. Ríos, Q. Du, Y. Zhang, C.-C. Popescu, M. Y. Shalaginov, P. Miller, C. Roberts, M. Kang, K. A. Richardson, T. Gu, *PhotoniX* **2022**, *3*, 26.
[52] W. Zhou, B. Dong, N. Farmakidis, X. Li, N. Youngblood, K. Huang, Y. He, C. D. Wright, W. H. Pernice, H. Bhaskaran, *Nat. Commun.* **2023**, *14*, 2887.
[53] P. Noé, C. Vallée, F. Hippert, F. Fillot, J.-Y. Raty, *Semicond. Sci. Technol.* **2017**, *33*, 013002.
[54] Z. Fang, R. Chen, J. Zheng, A. I. Khan, K. M. Neilson, S. J. Geiger, D. M. Callahan, M. G. Moebius, A. Saxena, M. E. Chen, *Nat. Nanotechnol.* **2022**, *17*, 842.
[55] M. Delaney, I. Zeimpekis, D. Lawson, D. W. Hewak, O. L. Muskens, *Adv. Funct. Mater.* **2020**, *30*, 2002447.
[56] Y. Miyatake, K. Makino, J. Tominaga, N. Miyata, T. Nakano, M. Okano, K. Toprasertpong, S. Takagi, M. Takenaka, *IEEE Trans. Electron Devices* **2023**, *70*, 2106.
[57] K. Ding, J. Wang, Y. Zhou, H. Tian, L. Lu, R. Mazzarello, C. Jia, W. Zhang, F. Rao, E. Ma, *Science* **2019**, *366*, 210.
[58] K. Ding, B. Chen, F. Rao, *Mater. Sci. Semicond. Process.* **2021**, *134*, 105999.
[59] M. Salinga, B. Kersting, I. Ronneberger, V. P. Jonnalagadda, X. T. Vu, M. L.e Gallo, I. Giannopoulos, O. Cojocaru-Mirédin, R. Mazzarello, A. Sebastian, *Nat. Mater.* **2018**, *17*, 681.
[60] Z. Cheng, T. Milne, P. Salter, J. S. Kim, S. Humphrey, M. Booth, H. Bhaskaran, *Sci. Adv.* **2021**, *7*, eabd7097.

[61] J. P. Perdew, K. Burke, M. Ernzerhof, *Phys. Rev. Lett.* **1996**, *77*, 3865.
[62] G. Kresse, J. Hafner, *Phys. Rev. B.* **1993**, *47*, 558.
[63] G. Kresse, J. Furthmüller, *Comput. Mater. Sci.* **1996**, *6*, 15.
[64] G. Kresse, J. Furthmüller, *Phys. Rev. B.* **1996**, *54*, 11169.
[65] G. Kresse, D. Joubert, *Phys. Rev. B.* **1999**, *59*, 1758.
[66] P. Giannozzi, S. Baroni, N. Bonini, M. Calandra, R. Car, C. Cavazzoni, D. Ceresoli, G. L. Chiarotti, M. Cococcioni, I. Dabo, *J. Phys.: Condens. Matter* **2009**, *21*, 395502.
[67] S. Grimme, J. Antony, S. Ehrlich, H. Krieg, *J. Chem. Phys.* **2010**, *132*, 154104.